Research Article

Seyyed Behnam Abdollahi Boraei, Jhamak Nourmohammadi, Fatemeh Sadat Mahdavi, Yasser Zare, Kyong Yop Rhee*, Ana Ferrández Montero, Antonio Javier Sánchez Herencia, and Begoña Ferrari*

# Osteogenesis capability of three-dimensionally printed poly(lactic acid)-halloysite nanotube scaffolds containing strontium ranelate

https://doi.org/10.1515/ntrev-2022-0113
received February 26, 2022; accepted April 22, 2022

**Abstract:** In this study, three-dimensional (3D) printing of 3D scaffolds containing halloysite nanotubes (HNTs) and strontium ranelate (SrR) as a carrier for the promotion of bone regeneration is investigated. SrR acts as an anabolic bone-forming and anti-catabolic agent, while HNTs act as a carrier of SrR. Poly(lactic acid) (PLA) is used as a biodegradable matrix and carrier for HNTs and SrR. The effects of the SrR addition on the morphological, biological, and *in vitro* release properties of the scaffolds are evaluated. The morphological results show a homogeneous structure with a proper pore size (approximately 400 μm) suitable for osteogenesis. The contact angle is decreased after the addition of SrR to the scaffold to 67.99°, suitable for cell attachment. X-ray diffraction shows that the SrR is homogenously and molecularly distributed in the PLA matrix and reduces the crystallinity in the prepared scaffolds. The *in vitro* release results demonstrate that the release profile of the SrR is stable, relatively linear, and continuous within 21 days (504 h). A cumulative release of SrR of approximately 49% is obtained after a controlled release for 504 h (21 days) and a low primary burst release (12%). Human adipose stem cells cultured on the 3D-printed scaffolds demonstrate that the SrR can efficiently promote biocompatibility, alkaline phosphatase activity, and alizarin red staining.

**Keywords:** bone regeneration, three-dimensional printing, strontium ranelate, halloysite nanotube, poly(lactic acid)

## 1 Introduction

In general, bone is a composite composition that has three main parts: matrix, fiber, and cell. The most important part is the collagen matrix, which bears the tensile mechanical loads, while the mineral phase, which consists of calcium phosphates, bears the compressive mechanical loads [1–4]. In this regard, the bone tissue experiences numerous defects throughout life, including problems caused by trauma, injuries of various origins, and aging, which are increasingly studied to address the related problems [5–9]. Considering the importance of these problems, bone tissue engineering is a new progressing method considered to mitigate osteogenesis [10–13]. Scaffolds are the most important part of tissue engineering science. The scaffold is a matrix in three-dimensional (3D) structures, which has essential characteristics, such as biocompatibility and proper mechanical properties, induces cellular activity and protein production, and provides cell attachment, differentiation, and proliferation [14–19]. The interconnecting pore is a significant factor for synthetic scaffolds in bone tissue engineering applications [20,21]. The pore sizes must be around 300 μm for good vascularization, cell attachment, and growth guidance in three dimensions [22]. Several methods are used to obtain porous scaffolds, such as solvent casting, foam gel method, freeze-drying, thermally induced

* **Corresponding author: Kyong Yop Rhee,** Department of Mechanical Engineering (BK21 Four), College of Engineering, Kyung Hee University, Yongin, Republic of Korea, e-mail: rheeky@khu.ac.kr
* **Corresponding author: Begoña Ferrari,** Institute of Ceramic and Glass, CSIC, C/Kelsen 5, 28010, Madrid, Spain, e-mail: bferrari@icv.csic.es
**Seyyed Behnam Abdollahi Boraei, Yasser Zare:** Biomaterials and Tissue Engineering Research Group, Department of Interdisciplinary Technologies, Breast Cancer Research Center, Motamed Cancer Institute, ACECR, Tehran, Iran
**Jhamak Nourmohammadi:** Department of Life Science Engineering, Faculty of New Sciences and Technologies, University of Tehran, Tehran, Iran
**Fatemeh Sadat Mahdavi:** Department of Biotechnology, University of Tehran, Tehran, Iran
**Ana Ferrández Montero, Antonio Javier Sánchez Herencia:** Institute of Ceramic and Glass, CSIC, C/Kelsen 5, 28010, Madrid, Spain

phase separation, particle/salt leaching, and chemical/gas foaming [23–29]. In recent years, additive manufacturing is widely used in bone repair applications.

Composite structures have been synthesized for various applications, which include ceramic, polymer, and metal compounds [30–37]. Polymer–ceramic nanocomposites with drug-loading properties are widely used in tissue engineering and in cases that require appropriate mechanical properties as well as controlled release of drugs [38,39]. Synthetic biopolymers, including poly(lactic acid) (PLA) and polycaprolactone, are useful for numerous applications in the synthesis of nanocomposites [40–47]. A 3D-printed PLA was investigated in recent years. PLA can be 3D printed at low temperatures, while the agent is bound by a binder solution [48–50]. In the 3D-printing method, biocompatible polymers can be used, and thus, composite scaffolds can be designed and manufactured [51]. The osteogenesis agent used in the matrix should be elucidated and its local release should be effective and beneficial. Among such agents, strontium ranelate (SrR), which has anabolic and anticatabolic properties, is increasingly used in tissue engineering scaffolds [52]. The addition of SrR increases the adhesion, proliferation, alkaline phosphatase (ALP) activity, mineralization, and angiogenesis of the 3D-printed scaffolds [53,54]. Another important factor of tissue engineering scaffolds containing drugs is the controlled release of the drug for a proper tissue regeneration. Halloysite nanotubes (HNTs) could help control the release of SrR and reduce its initial burst release [55]. HNT is a natural aluminosilicate that attracts considerable attention and has many applications [56–59]. HNT has unique properties, such as good mechanical and thermal properties, and is a suitable carrier of drugs. Several studies have been carried out on its applications and properties [60–64].

In this study, the 3D-printing technique was employed to obtain PLA/HNT-SrR scaffolds with different compounds (PLA, PLA/HNT, and PLA/HNT-SrR). The scaffold morphologies were evaluated by scanning electron microscopy (SEM). An X-ray diffraction (XRD) analysis was performed to elucidate the crystallographic features of the scaffolds. The drug release behavior of the SrR-loaded scaffolds was investigated. In addition, the cellular behaviors 3-(4,5-dimethylthiazol-2-yl)-2,5-diphenyltetrazolium bromide (MTT), ALP activity, and calcium assay of the 3D scaffolds were revealed.

# 2 Experimental section

## 2.1 Preparation and characterization of scaffolds

SrR was purchased from Servier Co. (UK). PLA (PLA 2003D, D-isomer content: 4.25%, Nature-Works LLC, Minnetonka, USA) and HNT (Sigma-Aldrich, St. Louis, USA) were used. Cetyltrimethylammonium bromide (CTAB, 99%) as a surfactant was purchased from Sigma-Aldrich. Fetal bovine serum, high-glucose Dulbecco's modified Eagle's medium (HG-DMEM), phosphate-buffered saline (PBS), and penicillin–streptomycin were purchased from GIBCO. Tetrahydrofuran (THF; purity: 99%, Panreac) was provided by Darmstadt Co. (Germany).

Suspensions of HNT- and SrR-modified HNT dispersed by adding 2 wt% CTAB (with respect to the solid content of HNT) in a PLA solution in THF (80 g/L) were prepared and granulated as described elsewhere [55,65]. Granules were crushed into fine powders for the extrusion of colloidal filaments and printing [66]. The 3D scaffold was obtained by a 3D-printing device (Prusa I3 with the Repetier software). 3D scaffolds with different compositions (PLA, PLA/HNT, and PLA/HNT-SrR) were printed (diameter: 1 cm, height: 0.2 cm, infill density: 40%, four layers). The prepared scaffolds were immersed in NaOH (20 wt%) for 5–10 s for a cross-linking treatment and then washed with deionized $H_2O$.

The PLA-based scaffolds were coated with gold (SC7620, QUOROMTECHNOLOGIES-EMITECH, England), and then, the microstructure was observed by SEM (AIS2100, SERON TECHNOLOGY, South Korea) in the secondary-electron mode at 20 kV to evaluate the morphology. Energy-dispersive spectrometry (EDS) was used to confirm the presence of HNTs and SrR in the scaffolds as well as their uniform distributions.

An attenuated total reflectance (ATR) Fourier-transform infrared (FTIR) analysis (Spectrum 100, PerkinElmer Company, UK) was used to investigate the functional groups and structural composition of the scaffolds.

The crystallography structures of the scaffolds were evaluated by XRD (EQUINOX3000, Inel, France) with Cu Kα radiation at a voltage of 40 kV and a scan rate of 2°/min.

The hydrophilicity of the scaffolds was evaluated by a contact angle analysis. Approximately 20 μL of distilled

water was dropped on a flat surface part of the scaffold. The contact angle was recorded after 2 s. A drop shape analysis software was applied to determine the baseline and contact angle. The results are presented as mean and standard deviation of five replications for each sample.

The release profile of SrR from the SrR-containing scaffold (0.5 g) was investigated by immersing the scaffold in 5 mL of PBS. It was then incubated in a shaker incubator at 90 rpm. At selected time points, 2 mL of the PBS was picked up and replaced with 2 mL of fresh PBS. The amount of released SrR was evaluated by an ultraviolet (UV)-visible device (NANODROP 2000c, Thermo Scientific Co., USA) at several time points (24, 48, 72, 120, 168, 336, and 504 h) at a wavelength of 318 nm.

## 2.2 Cellular assay

The prepared scaffolds were punched, placed into tissue culture polystyrene (TCPS), and then sterilized by 70% ethanol for 2 h and 20 min UV irradiation on each side. After immersing the scaffolds in a culture medium overnight, the density of primitive cells was $2 \times 10^5$ cells/cm$^2$. They were suspended in 200 µL of HG-DMEM and then seeded on the prepared scaffolds and controls (TCPS). The incubation was carried out for 30 min. Afterward, the basal medium (800 µL) was poured into the wells. All scaffolds were moved to new plates. The osteogenic medium was added and kept for 7 and 14 days. The renovation of the osteogenic medium was carried out every 2 days.

The cytotoxicity and viability of human adipose-derived stem cells (hASCs) on the prepared scaffolds were investigated by an MTT assay. The scaffolds were punched and placed into the plates. The primitive density of hASCs was $2 \times 10^5$ cells/cm$^2$. The plates were then placed into the incubator. Fifty microliters of the MTT solution (5 mg/mL) were then poured into the wells. The medium was removed after 2 h from the incubation. Three hundred microliters of dimethylsulfoxide (Merck) were then replaced to dissolute the dark-blue intracellular formazan. This procedure was carried out at the first, fourth, and seventh days of cell seeding. The dye solutions were then moved to six-well plates to observe the optical density of each well at 570 nm by a spectrophotometer (BioTek Instruments, USA).

Radioimmunoprecipitation assay buffer (200 µL) was used to extract the total protein from hASCs cultured on samples and TCPS for ALP activity evaluation at the time points of 7 and 14 days. The lysate was centrifuged (1,200 rpm, 4°C, 5 min) for the sedimentation of cell debris. An ALP assay kit (Parsazmun Co., Tehran, Iran) was used to measure the ALP activity of the collected supernatant.

The cresolphthalein complexone method was used to evaluate the amount of deposited calcium on the samples and TCPS. The homogenization of the hASCs was carried out by HCl (0.6 N, Merck Co.). They were shaken for 4 h at 4°C. In this stage, after the addition of a reagent to the calcium solution, the optical density was measured at 405 nm [38].

The mentioned analyses were carried out three times. Mean ± standard deviation was used to present the final data. The differences between the results were evaluated by a one-way analysis of variance. All results were statistically investigated at a level of $p < 0.05$.

# 3 Results and discussion

## 3.1 Characterization of the 3D-printed scaffolds

A proper scaffold provides specified features, such as a porous structure and interconnected pores for cell adhesion, proliferation, and differentiation, as well as transfer of nutrients to the cells and removal of waste products from cells [38]. Figure 1 shows SEM images of the 3D-printed scaffolds and macroporous structure. The homogeneous porous and completely interconnected matrix were detected in the scaffolds. According to the fixed setup of the printer, all samples have the same pore size (the mean value is 400 µm), which is in good agreement with other studies and in the suitable range for bone regeneration applications [67,68].

The increase in HNT content reduces the smoothness of the scaffold surface, mainly owing to the tendency of the nanoparticles for agglomeration at high concentrations [69]. HNT is stiffer than molten PLA, and thus, the polymer drags partially with the nozzle movement during the 3D printing [70].

To confirm the presence of HNTs and SrR in the scaffolds, an EDS analysis of Al, Si, and Sr elements was carried out on the scaffolds, as shown in Figure 2. The images show the uniform distribution of HNTs (Al and Si elements) and SrR (Sr element) in the PLA matrix.

Figure 3 shows the results of the ATR FTIR spectroscopy of the scaffolds. The typical bands of PLA (polyesters) are observed, including those at 2,921 and 2,851 cm$^{-1}$

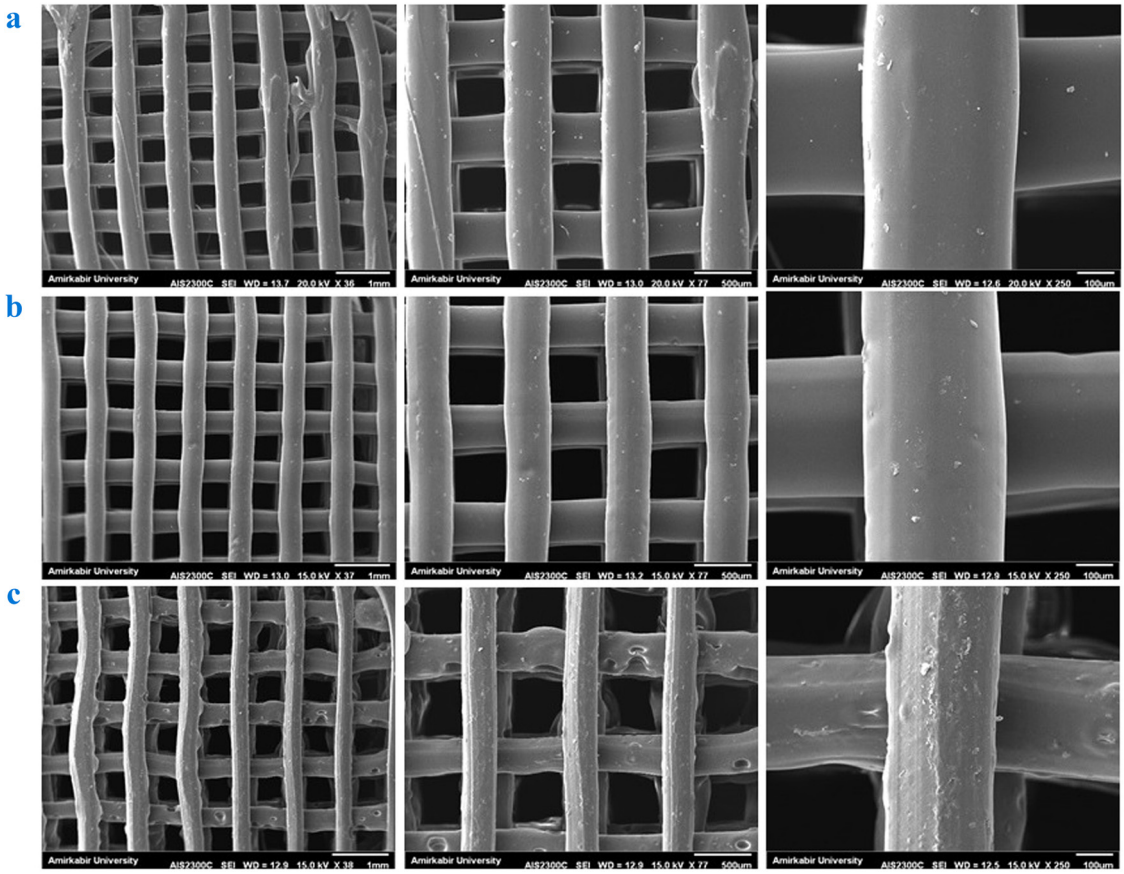


**Figure 1:** SEM images of (a) PLA, (b) PLA/HNT, and (c) PLA/HNT-SrR scaffolds at various magnifications.

attributed to symmetric and asymmetric vibrations of the C–H bond of the $CH_3$ groups, respectively, at 1,741 and 1,179 $cm^{-1}$ related to C═O and C–O–C stretching, respectively, at 1,450 $cm^{-1}$ corresponding to C–H stretching vibration in methyl groups, at 1,363 $cm^{-1}$ assigned to symmetric vibrations of –CH– bending, at 1,076 $cm^{-1}$ related to carbonyl C═O and –OH groups, and at 867 and 753 $cm^{-1}$ assigned to the C–C stretching vibration in the structure [71,72]. After the addition of HNTs to the structure, the bands at 2,851 and 2,925 $cm^{-1}$ attributed to PLA slightly shifted to higher wavenumbers, which indicates hydrogen bonding of the hydroxyl chains of PLA with the siloxane groups of halloysites. The band at 1,023 $cm^{-1}$ corresponds to the stretching of the Si–O group, which indicates the successful incorporation of the HNT in the structure [73]. After the loading of SrR, bands at 1,260 and 1,355 $cm^{-1}$ appeared, which are related to the C–N vibration in SrR. This indicates a successful loading of the SrR drug into the scaffold structure.

Figure 4 shows XRD results of the prepared scaffolds. In general, they have two characteristic peaks at $2\theta$ of 17° and 19° [74]. A similar peak is observed in our results ($2\theta$ = 16.72°) but is too broad, which indicates that the PLA is amorphous during the scaffold preparation. The HNTs usually have several specific peaks. In this study, owing to the low percentage of HNTs in the structure of the scaffolds, not all of their peaks are clear. Only the characteristic peak at $2\theta$ = 12.05° for the PLA/HNT scaffold, which contains HNTs, is observed. This peak is similar to the major peak of HNTs at $2\theta$ = 11.9° [75]. The peak demonstrates the presence of HNTs in the structure. This peak is in good agreement with the (001) basal plane of HNTs [68]. After the addition of SrR to the structure, no characteristic peaks of SrR were observed owing to two reasons: (1) low percentage of SrR in the scaffold, which makes it undetectable for the device, and (2) with the addition of SrR to the polyesters and polyethers that compose the scaffold matrix, the crystallinity of the SrR is reduced, and thus, it tends to become amorphous [39].

The contact angle test results of the PLA, PLA/HNT, and PLA/HNT-SrR scaffolds are presented in Figure 5. As expected, the contact angle of the PLA scaffold was the largest, 111.1 ± 13.63°, which is in the range reported for polyesters [76]. Upon the addition of HNTs to the

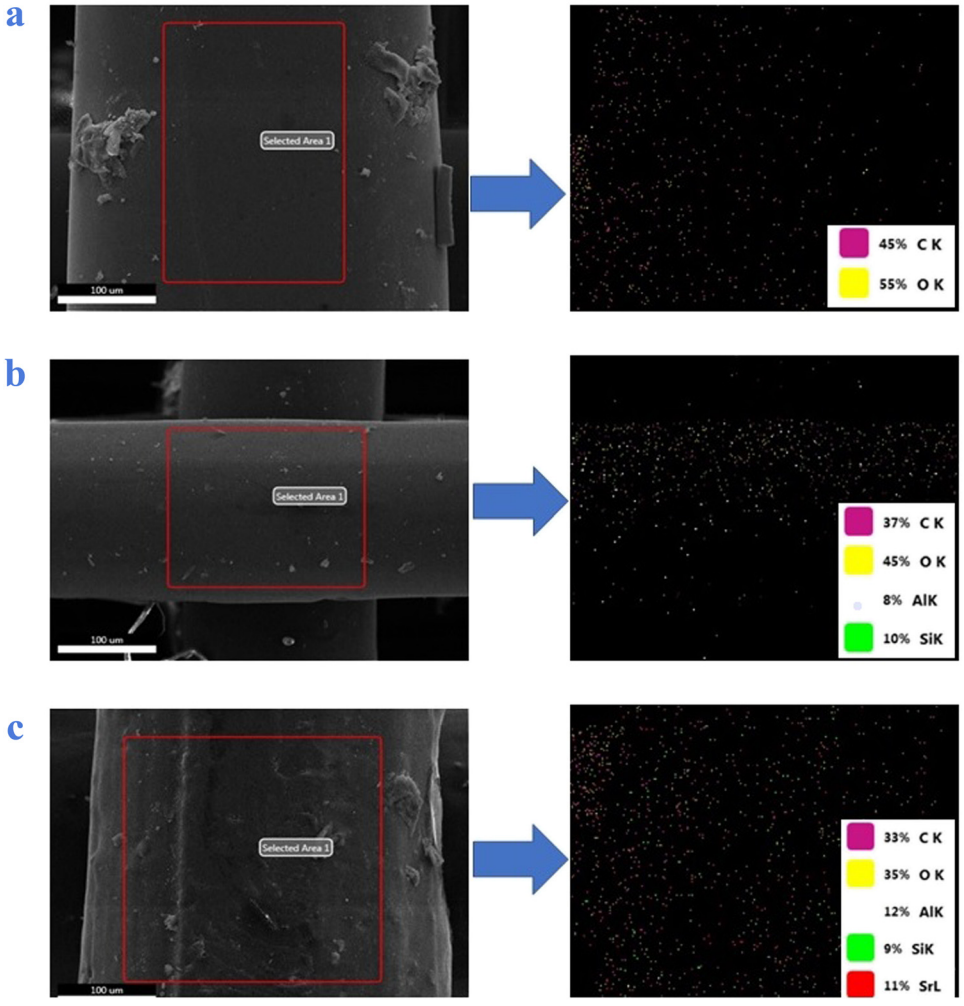


**Figure 2:** EDS analyses of the (a) PLA, (b) PLA/HNT, and (c) PLA/HNT-SrR scaffolds.

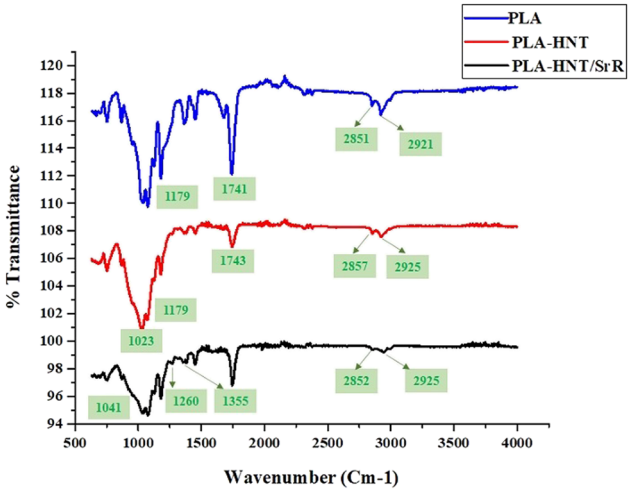


**Figure 3:** FTIR spectra of the prepared scaffolds.

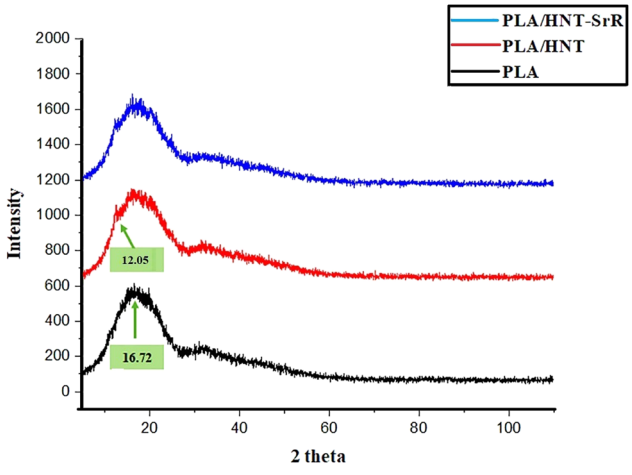


**Figure 4:** XRD patterns of the PLA, PLA/HNT, and PLA/HNTs-SrR scaffolds.

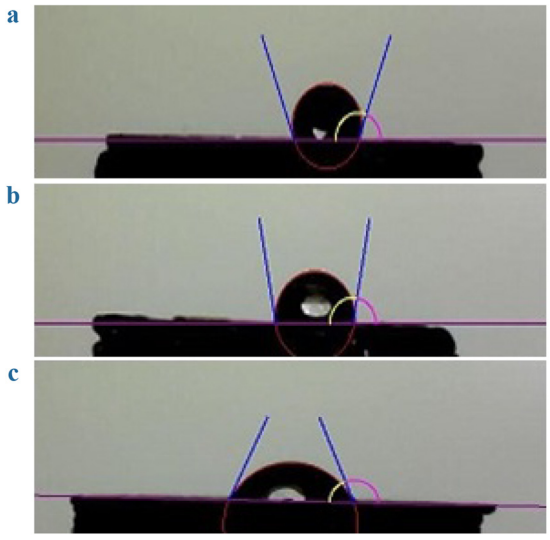


**Figure 5:** Contact angle results of the (a) PLA, (b) PLA/HNT, and (c) PLA/HNT-SrR scaffolds.

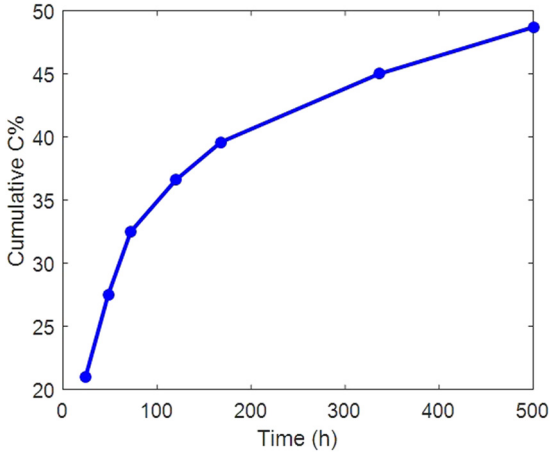


**Figure 6:** Release behavior of the PLA/HNT-SrR scaffold in PBS.

structure, the contact angle and hydrophobicity of the structure are reduced (100.15 ± 11.23°). After the addition of SrR to the structure, which is a completely hydrophilic drug, the hydrophobicity of the structure was reduced and the angle reached 67.99 ± 5.47°. In general, with the increase in the amount of hydrophilic components in the structure (in this case, SrR), a decrease in contact angle is expected. The suitable contact angle range for the hydrophilicity of scaffolds and cell attachment to the scaffold is 40–70°, considered an important parameter [39,77].

## 3.2 *In vitro* SrR release investigations

Figure 6 shows the release profiles of SrR from the scaffolds. The HNT was added as a drug carrier to the scaffold to control the release behavior of the SrR. Twenty-one days (500 h) is a suitable time for osteogenesis differentiation by continuous release of SrR. The porous 3D scaffold exhibited a relatively linear and stable release behavior of SrR. The cumulative release after 500 h was approximately 49%, similar to our previous result [38]. Owing to the formation of SrR bonds on or into the HNT, the SrR release profile exhibits a controlled behavior. As shown in Figure 6, the initial burst release rate of SrR from the scaffold is extremely low, approximately 12%. The initial burst release is very high in many systems, particularly in systems without drug carriers. In general, two mechanisms can be proposed for the release of SrR from HNT-containing nanocomposite scaffolds. The first mechanism is attributed to siloxane groups (Si–O–Si) on the HNT surface and their negative charge. Thus, they can bond the positively charged strontium. The second mechanism is attributed to aluminum hydroxide groups ($Al(OH)_2$) inside the positively charged HNT lumens. Thus, there is a possibility of bond formation between them and the negative terminal of the ranelate [55].

## 3.3 Cellular analysis

Biocompatibility and nontoxicity are important factors for a good scaffold. An MTT assay was performed to investigate the cytocompatibility of the prepared samples by culturing hASCs on them (Figure 7). The proliferation of hASCs on the SrR-containing scaffold after 1, 4, and 7 days was better than those for the PLA and PLA/HNT samples. After 5 days, it was better in the case with the SrR scaffold than for the other samples. The extracts acquired from the PLA/HNT and PLA/HNT-SrR scaffolds exhibited superior cell viabilities after 1, 4, and 7 days [78]. Thus, all prepared scaffolds in our experiment exhibited a good cytocompatibility and were suitable for bone tissue engineering. The results of the MTT analysis can be explained using the EDS analysis, where the scaffold containing the drug and element strontium exhibited a higher cell proliferation, as expected.

The ALP activity was evaluated to investigate the osteogenic potential of the cells. ALP is an important osteogenic marker expressed in the early stages. The results showed an increase in the ALP activity. Despite the release of SrR, it does not have a significant effect on the hASCs growth in the first week. There is a notable difference between the SrR-containing scaffolds and the

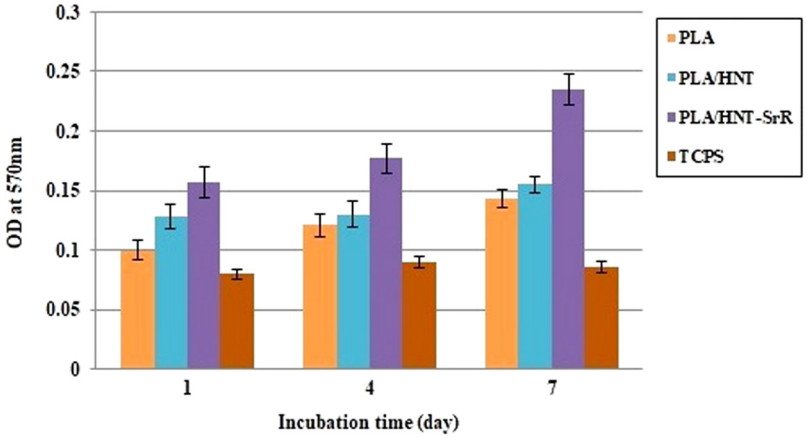


**Figure 7:** MTT assays of cell proliferation and viability on the scaffolds.

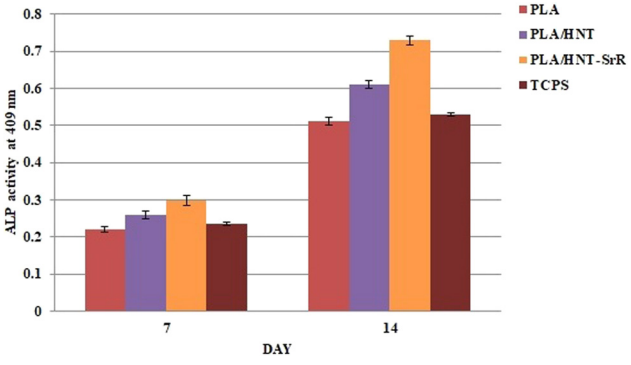


**Figure 8:** ALP activity of the hASCs on the prepared scaffolds ($p < 0.05$).

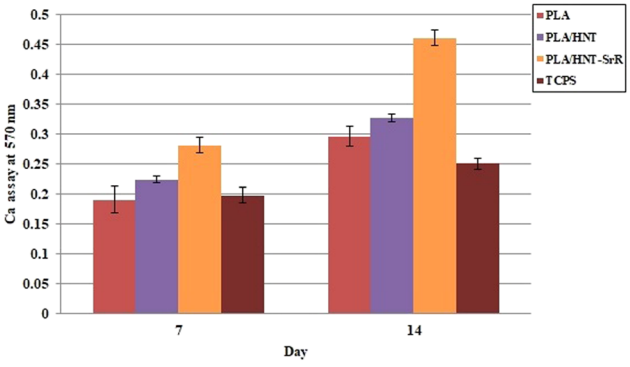


**Figure 9:** ARS of culture hASCs on the scaffolds at different times.

rest of scaffolds in the second week [38]. Figure 8 shows a higher ALP activity in the PLA/HNT-SrR scaffold than in the PLA and PLA/HNT scaffolds at day 14 ($p < 0.05$). These results are consistent with the contact angle analysis, where the scaffold containing SrR had the optimal contact angle and consequently higher hydrophilicity, which, in turn, increased the cell attachment and improved the APL results.

In general, large amounts of calcium deposits are observed in bone tissue. Alizarin red staining (ARS) is one of the approved evaluation methods for calcium deposition and subsequent mineralization of synthesized scaffolds. In this study, such a test was performed after 7 and 14 days. Figure 9 shows an increase in the calcium content after 14 days of culturing, higher than that after 7 days. The scaffold containing SrR exhibited the highest amount on day 7 and the highest increase on day 14. The SrR-containing scaffold had the largest amount of deposits among the prepared scaffolds [79]. As shown in Figure 9, the ARS quantification indicates that the deposition of calcium in the SrR porous scaffold was considerably higher than that in the neat scaffold. Hence, the SrR-containing scaffold accelerates the bone formation-enhanced osteogenic differentiation. Several mechanisms about the osteogenesis ability of SrR have been investigated [80–82].

# 4 Conclusion

The 3D-printing technology was used to produce proper scaffolds for bone tissue engineering applications. Interconnected porous structures with pore sizes of approximately 400 µm and high porosities were produced. The addition of SrR to the scaffolds remarkably changed the properties of the 3D-printed scaffolds. A cumulative release of SrR of approximately 49% was obtained after the controlled release for 504 h (21 days) and low primary burst release (12%). The sustained release of SrR could be observed for at least 504 h (21 days) owing to the loading of SrR on or into the HNTs. The contact angle largely decreased upon the

addition of SrR to the structure to 67.99° in a suitable range for cell attachment. The nontoxicity of HNT and SrR was demonstrated after their addition to the PLA scaffold. The cellular analysis demonstrated that the ALP activity and calcium deposition increased upon the addition of SrR to the scaffold. Thus, the produced scaffolds can provide a good porous 3D structure in bone tissue engineering applications and prompt bone regeneration.

**Funding information:** This work was supported by the Basic Science Research Program through the National Research Foundation of Korea (NRF) funded by the Ministry of Education, Science and Technology (project number: 2022R1A2C1004437).

**Author contributions:** All authors have accepted responsibility for the entire content of this manuscript and approved its submission.

**Conflict of interest:** The authors state no conflict of interest.

## References

[1] Wei S, Ma J-X, Xu L, Gu X-S, Ma X-L. Biodegradable materials for bone defect repair. Mil Med Res. 2020;7(1):1–25.
[2] Wang W, Zhang B, Zhao L, Li M, Han Y, Wang L, et al. Fabrication and properties of PLA/nano-HA composite scaffolds with balanced mechanical properties and biological functions for bone tissue engineering application. Nanotechnol Rev. 2021;10(1):1359–73.
[3] Wang J, Zhang Y, Yang X, Ma X. Stress effect on 3D culturing of MC3T3-E1 cells on microporous bovine bone slices. Nanotechnol Rev. 2020;9(1):1315–25.
[4] Xing F, Zhou C, Hui D, Du C, Wu L, Wang L, et al. Hyaluronic acid as a bioactive component for bone tissue regeneration: Fabrication, modification, properties, and biological functions. Nanotechnol Rev. 2020;9(1):1059–79.
[5] Preethi A, Bellare JR. Tailoring scaffolds for orthopedic application with anti-microbial properties: current scenario and future prospects. Front Mater. 2021;452:1–24.
[6] Abbasi N, Hamlet S, Love RM, Nguyen N-T. Porous scaffolds for bone regeneration. J Sci Adv Mater Devices. 2020;5(1):1–9.
[7] Cunniffe GM, O'Brien FJ. Collagen scaffolds for orthopedic regenerative medicine. JOM. 2011;63(4):66–73.
[8] Huo Y, Lu Y, Meng L, Wu J, Gong T, Zou JA, et al. A critical review on the design, manufacturing and assessment of the bone scaffold for large bone defects. Front Bioeng Biotechnol. 2021;946:1–13.
[9] Yang YP, Labus KM, Gadomski BC, Bruyas A, Easley J, Nelson B, et al. Osteoinductive 3D printed scaffold healed 5 cm segmental bone defects in the ovine metatarsus. Sci Rep. 2021;11(1):1–12.
[10] Koons GL, Diba M, Mikos AG. Materials design for bone-tissue engineering. Nat Rev Mater. 2020;5(8):584–603.
[11] Qu H, Fu H, Han Z, Sun Y. Biomaterials for bone tissue engineering scaffolds: a review. RSC Adv. 2019;9(45):26252–62.
[12] Kargozar S, Mozafari M, Hamzehlou S, Brouki Milan P, Kim H-W, Baino F. Bone tissue engineering using human cells: a comprehensive review on recent trends, current prospects, and recommendations. Appl Sci. 2019;9(1):174.
[13] Perić Kačarević Ž, Rider P, Alkildani S, Retnasingh S, Pejakić M, Schnettler R, et al. An introduction to bone tissue engineering. Int J Artif Organs. 2020;43(2):69–86.
[14] Hu C, Wu L, Zhou C, Sun H, Gao P, Xu X, et al. Berberine/Ag nanoparticle embedded biomimetic calcium phosphate scaffolds for enhancing antibacterial function. Nanotechnol Rev. 2020;9(1):568–79.
[15] Radakisnin R, Majid MSA, Jamir MRM, Tahir MFM, Meng CE, Al Alshahrani H. Physical, thermal, and mechanical properties of highly porous polylactic acid/cellulose nanofibre scaffolds prepared by salt leaching technique. Nanotechnol Rev. 2021;10(1):1469–83.
[16] Zhang L, Zheng T, Wu L, Han Q, Chen S, Kong Y, et al. Fabrication and characterization of 3D-printed gellan gum/starch composite scaffold for Schwann cells growth. Nanotechnol Rev. 2021;10(1):50–61.
[17] Peng Z, Tang P, Zhao L, Wu L, Xu X, Lei H, et al. Advances in biomaterials for adipose tissue reconstruction in plastic surgery. Nanotechnol Rev. 2020;9(1):385–95.
[18] Ahmed M, Menazea A, Mansour S, Al-Wafi R. Differentiation between cellulose acetate and polyvinyl alcohol nanofibrous scaffolds containing magnetite nanoparticles/graphene oxide via pulsed laser ablation technique for tissue engineering applications. J Mater Res Technol. 2020;9(5):11629–40.
[19] Mosaddad SA, Yazdanian M, Tebyanian H, Tahmasebi E, Yazdanian A, Seifalian A, et al. Fabrication and properties of developed collagen/strontium-doped Bioglass scaffolds for bone tissue engineering. J Mater Res Technol. 2020;9(6):14799–817.
[20] Lutzweiler G, Ndreu Halili A, Engin, Vrana N. The overview of porous, bioactive scaffolds as instructive biomaterials for tissue regeneration and their clinical translation. Pharmaceutics. 2020;12(7):602.
[21] Arastouei M, Khodaei M, Atyabi SM, Nodoushan MJ. Poly lactic acid-akermanite composite scaffolds prepared by fused filament fabrication for bone tissue engineering. J Mater Res Technol. 2020;9(6):14540–8.
[22] Karageorgiou V, Kaplan D. Porosity of 3D biomaterial scaffolds and osteogenesis. Biomaterials. 2005;26(27):5474–91.
[23] Cao H, Kuboyama N. A biodegradable porous composite scaffold of PGA/β-TCP for bone tissue engineering. Bone. 2010;46(2):386–95.
[24] Kucharska M, Butruk B, Walenko K, Brynk T, Ciach T. Fabrication of in-situ foamed chitosan/β-TCP scaffolds for bone tissue engineering application. Mater Lett. 2012;85:124–7.
[25] Sultana N, Wang M. Fabrication of HA/PHBV composite scaffolds through the emulsion freezing/freeze-drying process and characterisation of the scaffolds. J Mater Sci Mater Med. 2008;19(7):2555.
[26] Yoshikawa H, Tamai N, Murase T, Myoui A. Interconnected porous hydroxyapatite ceramics for bone tissue engineering. J R Soc Interface. 2009;6(Suppl 3):S341–8.

[27] Hutmacher DW. Scaffolds in tissue engineering bone and cartilage. The biomaterials: Silver Jubilee Compendium. Elsevier: Amsterdam, Netherlands; 2006. p. 175–89.
[28] Collins MN, Ren G, Young K, Pina S, Reis RL, Oliveira JM. Scaffold fabrication technologies and structure/function properties in bone tissue engineering. Adv Funct Mater. 2021;31(21):2010609.
[29] Hu X, Yang Z, Kang S, Jiang M, Zhou Z, Gou J, et al. Cellulose hydrogel skeleton by extrusion 3D printing of solution. Nanotechnol Rev. 2020;9(1):345–53.
[30] Zare Y, Rhee KY. Tensile modulus prediction of carbon nanotubes-reinforced nanocomposites by a combined model for dispersion and networking of nanoparticles. J Mater Res Technol. 2019;9:22–32.
[31] Zare Y, Rhee KY. Analysis of critical interfacial shear strength between polymer matrix and carbon nanotubes and its impact on the tensile strength of nanocomposites. J Mater Res Technol. 2020;9:4123–32.
[32] Abdollahi Boraei SB, Esmaeili Bidhendib M, Afzali D. Preparation of SiO2/ZrO2 ceramic nanocomposite coating on aluminum alloys as metallic part of the photovoltaic cells and study its corrosion behavior. Environ Energy Economic Res. 2017;1(2):231–8.
[33] Abdollahi B, Afzali D, Hassani Z. Corrosion inhibition properties of SiO2-ZrO2 nanocomposite coating on carbon steel 178. Anti-Corr Methods Mater. 2018;65:66–72.
[34] Bayat H, Fasihi M, Zare Y, Rhee KY. An experimental study on one-step and two-step foaming of natural rubber/silica nanocomposites. Nanotechnol Rev. 2020;9(1):427–35.
[35] Naghib SM, Behzad F, Rahmanian M, Zare Y, Rhee KY. A highly sensitive biosensor based on methacrylated graphene oxide-grafted polyaniline for ascorbic acid determination. Nanotechnol Rev. 2020;9(1):760–7.
[36] Zare Y, Rhee KY. Development of Hashin-Shtrikman model to determine the roles and properties of interphases in clay/$CaCO_3$/PP ternary nanocomposite. Appl Clay Sci. 2017;137:176–82.
[37] Zare Y. Modeling approach for tensile strength of interphase layers in polymer nanocomposites. J Colloid Interface Sci. 2016;471:89–93.
[38] Abdollahi Boraei SB, Nourmohammadi J, Bakhshandeh B, Dehghan MM, Gonzalez Z, Ferrari B. The effect of protelos content on the physicochemical, mechanical and biological properties of gelatin-based scaffolds. J Appl Biotechnol Rep. 2020;7(1):41–7.
[39] Boraei SBA, Nourmohammadi J, Bakhshandeh B, Dehghan MM, Gholami H, Gonzalez Z, et al. Capability of core-sheath polyvinyl alcohol–polycaprolactone emulsion electrospun nanofibrous scaffolds in releasing strontium ranelate for bone regeneration. Biomed Mater. 2021;16(2):025009.
[40] Moradi S, Yeganeh JK. Highly toughened poly (lactic acid)(PLA) prepared through melt blending with ethylene-co-vinyl acetate (EVA) copolymer and simultaneous addition of hydrophilic silica nanoparticles and block copolymer compatibilizer. Polym Test. 2020;91:106735.
[41] Lohrasbi P, Yeganeh JK. Synergistic toughening of poly (lactic acid)/poly (ethylene vinyl acetate)(PLA/EVA) by dynamic vulcanization and presence of hydrophobic nanoparticles. Polym Adv Technol. 2021;32(11):4326–39.
[42] Rashedi S, Afshar S, Rostami A, Ghazalian M, Nazockdast H. Co-electrospun poly (lactic acid)/gelatin nanofibrous scaffold prepared by a new solvent system: morphological, mechanical and *in vitro* degradability properties. Int J Polym Mater Polym Biomater. 2021;70(8):545–53.
[43] Ghazalian M, Afshar S, Rostami A, Rashedi S, Bahrami SH. Fabrication and characterization of chitosan-polycaprolactone core-shell nanofibers containing tetracycline hydrochloride. Colloids Surf A Physicochem Eng Asp. 2022;636:128163.
[44] Tajdari A, Babaei A, Goudarzi A, Partovi R, Rostami A. Hybridization as an efficient strategy for enhancing the performance of polymer nanocomposites. Polym Compos. 2021;42(12):6801–15.
[45] Rostami A, Vahdati M, Alimoradi Y, Karimi M, Nazockdast H. Rheology provides insight into flow induced nano-structural breakdown and its recovery effect on crystallization of single and hybrid carbon nanofiller filled poly (lactic acid). Polymer. 2018;134:143–54.
[46] Rostami A, Nazockdast H, Karimi M. Graphene induced microstructural changes of PLA/MWCNT biodegradable nanocomposites: rheological, morphological, thermal and electrical properties. RSC Adv. 2016;6(55):49747–59.
[47] Zare Y, Garmabi H, Rhee KY. Structural and phase separation characterization of poly (lactic acid)/poly (ethylene oxide)/carbon nanotube nanocomposites by rheological examinations. Compos Part B Eng. 2018;144:1–10.
[48] Gbureck U, Hölzel T, Klammert U, Würzler K, Müller FA, Barralet JE. Resorbable dicalcium phosphate bone substitutes prepared by 3D powder printing. Adv Funct Mater. 2007;17(18):3940–5.
[49] Igawa K, Mochizuki M, Sugimori O, Shimizu K, Yamazawa K, Kawaguchi H, et al. Tailor-made tricalcium phosphate bone implant directly fabricated by a three-dimensional ink-jet printer. J Artif Organs. 2006;9(4):234–40.
[50] Butscher A, Bohner M, Roth C, Ernstberger A, Heuberger R, Doebelin N, et al. Printability of calcium phosphate powders for three-dimensional printing of tissue engineering scaffolds. Acta Biomater. 2012;8(1):373–85.
[51] Vorndran E, Klammert U, Ewald A, Barralet JE, Gbureck U. Simultaneous immobilization of bioactives during 3D powder printing of bioceramic drug-release matrices. Adv Funct Mater. 2010;20(10):1585–91.
[52] Nair BP, Sindhu M, Nair PD. Polycaprolactone-laponite composite scaffold releasing strontium ranelate for bone tissue engineering applications. Colloids Surf B Biointerf. 2016;143:423–30.
[53] Zhao S, Zhang J, Zhu M, Zhang Y, Liu Z, Tao C, et al. Three-dimensional printed strontium-containing mesoporous bioactive glass scaffolds for repairing rat critical-sized calvarial defects. Acta Biomater. 2015;12:270–80.
[54] Zhang W, Shi W, Wu S, Kuss M, Jiang X, Untrauer JB, et al. 3D printed composite scaffolds with dual small molecule delivery for mandibular bone regeneration. Biofabrication. 2020;12(3):035020.
[55] Boraei SBA, Nourmohammadi J, Mahdavi FS, Yus J, Ferrandez-Montero A, Sanchez-Herencia AJ, et al. Effect of SrR delivery in the biomarkers of bone regeneration during the *in vitro* degradation of HNT/GN coatings prepared by EPD. Colloids Surf B Biointerf. 2020;190:110944.
[56] Zare Y, Rhee KY. The strengthening efficacy of filler/interphase network in polymer halloysite nanotubes system after mechanical percolation. J Mater Res Technol. 2021;15:5343–52.

[57] Zare Y, Rhee KY, Park S-J. An applicable model for the modulus of polymer halloysite nanotubes samples by the characteristics of halloysite nanotubes, interphase zone and filler/interphase network. Colloids Surf A Physicochem Eng Asp. 2021;628:127330.
[58] Zhang R, Li Y, He Y, Qin D. Preparation of iodopropynyl butycarbamate loaded halloysite and its anti-mildew activity. J Mater Res Technol. 2020;9(5):10148–56.
[59] Zhang M, Wang L, Yan H, Lian L, Si J, Long Z, et al. Palladium-halloysite nanocomposites as an efficient heterogeneous catalyst for acetylene hydrochlorination. J Mater Res Technol. 2021;13:2055–65.
[60] Satish S, Tharmavaram M, Rawtani D. Halloysite nanotubes as a nature's boon for biomedical applications. Nanobiomedicine. 2019;6:1849543519863625.
[61] Santos AC, Pereira I, Reis S, Veiga F, Saleh M, Lvov Y. Biomedical potential of clay nanotube formulations and their toxicity assessment. Expert Opin Drug Deliv. 2019;16(11):1169–82.
[62] Danyliuk N, Tomaszewska J, Tatarchuk T. Halloysite nanotubes and halloysite-based composites for environmental and biomedical applications. J Mol Liq. 2020;309:113077.
[63] Zare Y, Rhee KY. Expansion of Takayanagi model by interphase characteristics and filler size to approximate the tensile modulus of halloysite-nanotube-filled system. J Mater Res Technol. 2021;16:1628–36.
[64] Zare Y, Rhee KY. A simple model for determining the strength of polymer halloysite nanotube systems. Compos Part B Eng. 2021;227:109411.
[65] Ferrández-Montero A, Eguiluz A, Vazquez E, Guerrero JD, Gonzalez Z, Sanchez-Herencia AJ, et al. Controlled SrR delivery by the incorporation of Mg particles on biodegradable PLA-based composites. Polymers. 2021;13(7):1061.
[66] Ferrández-Montero A, Ferrari-Fernández B, Sánchez Herencia AJ, González Granados Z, González López FJ, Yus J, et al. Method for obtaining a piece by fused filament deposition modelling. Cynical Technologic de Materials; 2019;224:1–9.
[67] Ghaee A, Nourmohammadi J, Danesh P. Novel chitosan-sulfonated chitosan-polycaprolactone-calcium phosphate nanocomposite scaffold. Carbohydr Polym. 2017;157:695–703.
[68] Abdollahi Boraei SB, Nourmohammadi J, Bakhshandeh B, Dehghan MM, Gholami H, Calle Hernández D, et al. Enhanced osteogenesis of gelatin-halloysite nanocomposite scaffold mediated by loading strontium ranelate. Int J Polym Mater Polym Biomater. 2021;70(6):392–402.
[69] Zare Y, Rhee KY. A simulation work for the influences of aggregation/agglomeration of clay layers on the tensile properties of nanocomposites. JOM. 2019;71:3989–95.
[70] Alam F, Verma P, Mohammad W, Teo J, Varadarajan K, Kumar S. Architected poly (lactic acid)/poly (ε-caprolactone)/halloysite nanotube composite scaffolds enabled by 3D printing for biomedical applications. J Mater Sci. 2021;56:1–14.
[71] Redondo FL, Giaroli MC, Ciolino AE, Ninago MD. Preparation of porous poly (lactic acid)/tricalcium phosphate composite scaffolds for tissue engineering. Biointerface Res Appl Chem; 2021;12:5610–24.
[72] Mofokeng JP, Luyt A, Tábi T, Kovács J. Comparison of injection moulded, natural fibre-reinforced composites with PP and PLA as matrices. J Thermop Compos Mater. 2012;25(8):927–48.
[73] Dong Y, Marshall J, Haroosh HJ, Mohammadzadehmoghadam S, Liu D, Qi X, et al. Polylactic acid (PLA)/halloysite nanotube (HNT) composite mats: Influence of HNT content and modification. Compos Part A Appl Sci Manuf. 2015;76:28–36.
[74] Hezma A, Abdelrazzak AB, El-Bahy GS. Preparation and spectroscopic investigations of hydroxyapatite-curcumin nanoparticles-loaded polylactic acid for biomedical application. Egypt J Basic Appl Sci. 2019;6(1):1–9.
[75] Divi MKP, Rao MAN, Nowshuddin S. Polymorph of strontium ranelate and a process for its preparation. Google Patents; 2011. US20110275834A1.
[76] Li X, Xie J, Yuan X, Xia Y. Coating electrospun poly (ε-caprolactone) fibers with gelatin and calcium phosphate and their use as biomimetic scaffolds for bone tissue engineering. Langmuir. 2008;24(24):14145–50.
[77] Chuah YJ, Koh YT, Lim K, Menon NV, Wu Y, Kang Y. Simple surface engineering of polydimethylsiloxane with polydopamine for stabilized mesenchymal stem cell adhesion and multipotency. Sci Rep. 2015;5(1):1–12.
[78] Zhao Y, Guo D, Hou S, Zhong H, Yan J, Zhang C, et al. Porous allograft bone scaffolds: doping with strontium. PLoS One. 2013;8(7):e69339.
[79] Su W-T, Wu P-S, Huang T-Y. Osteogenic differentiation of stem cells from human exfoliated deciduous teeth on poly (ε-caprolactone) nanofibers containing strontium phosphate. Mater Sci Eng C. 2015;46:427–34.
[80] Pilmane M, Salma-Ancane K, Loca D, Locs J, Berzina-Cimdina L. Strontium and strontium ranelate: historical review of some of their functions. Mater Sci Eng C. 2017;78:1222–30.
[81] Chen Y, Zheng Z, Zhou R, Zhang H, Chen C, Xiong Z, et al. Developing a strontium-releasing graphene oxide-/collagen-based organic–inorganic nanobiocomposite for large bone defect regeneration via MAPK signaling pathway. ACS Appl Mater Interfaces. 2019;11(17):15986–97.
[82] Caverzasio J, Thouverey C. Activation of FGF receptors is a new mechanism by which strontium ranelate induces osteoblastic cell growth. Cell Physiol Biochem. 2011;27(3–4):243–50.